

Physically Feasible Semantic Segmentation

Shamik Basu

University Of Bologna, Italy

shamik.basu@studio.unibo.it

Luc Van Gool

ETH Zurich

vangool@vision.ee.ethz.ch

Christos Sakaridis

ETH Zurich

csakarid@vision.ee.ethz.ch

Abstract

State-of-the-art semantic segmentation models are typically optimized in a data-driven fashion, minimizing solely per-pixel classification objectives on their training data. This purely data-driven paradigm often leads to absurd segmentations, especially when the domain of input images is shifted from the one encountered during training. For instance, state-of-the-art models may assign the label “road” to a segment which is located above a segment that is respectively labeled as “sky”, although our knowledge of the physical world dictates that such a configuration is not feasible for images captured by forward-facing upright cameras. Our method, Physically Feasible Semantic Segmentation (PhyFea), extracts explicit physical constraints that govern spatial class relations from the training sets of semantic segmentation datasets and enforces a differentiable loss function that penalizes violations of these constraints to promote prediction feasibility. PhyFea yields significant performance improvements in mIoU over each state-of-the-art network we use as baseline across ADE20K, Cityscapes and ACDC, notably a 1.5% improvement on ADE20K and a 2.1% improvement on ACDC. The code is at <https://github.com/SHAMIK-97/valeo>

1. Introduction

Semantic segmentation is a fundamental task in computer vision and enables many downstream applications. It is a classification problem, done at pixel level. This relationship is pointed out and systematically studied in a seminal work [15], where the authors used fully convolutional networks (FCNs) for semantic segmentation tasks. Since then, FCN has inspired many follow-up works and has become a predominant design choice for dense prediction. Since there is a strong relation between classification and semantic segmentation, many state-of-the-art semantic segmentation frameworks are variants of popular architectures for image classification on ImageNet, and many modern architectures use backbones for their architecture pre-trained with ImageNet.

Therefore, designing backbone architectures has remained an active area in semantic segmentation. Indeed, starting from early methods using VGGs [1, 15], to the latest methods with significantly deeper and more powerful backbones [2, 8, 14, 24, 27, 29, 31], the evolution of backbones has dramatically pushed the performance boundary of semantic segmentation, specially after the invention of ResNet [29] architectures. Besides backbone architectures, another line of work formulates semantic segmentation as a structured prediction problem, and focuses on designing modules and operators, which can effectively capture contextual information.

In a way we can say that the problem can be boiled down to the question of what? and where? at the pixel level. In this paper, we tried to correct mislabeled erroneous pixels, but in a different way. Here we tried to correct them by enforcing two physical priors into the model while training. This can be seen as training the architecture with the guidance of physical world knowledge. This paper work do not concern on building any new architecture to perform semantic segmentation rather, we have taken existing semantic segmentation models (we call it the baselines) SegFormer-B4 [26] and OCRNet without SegFix [28] and tried to enforce physical priors onto the prediction while re-training.

We have identified two physical anomalies in the predictions of our baseline model SegFormer-B4 on Cityscapes [7]. The physical anomalies, termed as physical world knowledge violations, are *infeasible inclusions* and *discontinued segments*.

1.1. Infeasible Inclusions

By infeasible inclusions we refer to those scenarios where a class segment is infeasibly surrounded by another class, e.g. road surrounded by sidewalk. Fig. 1 shows two such examples from the Cityscapes [7] validation set, which correspond to semantic predictions with SegFormer-B4 [26] and demonstrate clear violations of physical world knowledge, as a road segment which would be completely surrounded by sidewalk would not be accessible from the rest of the road network and a sidewalk cannot lie in the middle of a wall. However, not all inclusions are infeasible.

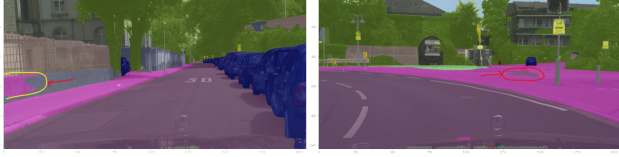


Figure 1. Left: a part of the wall is mislabelled as sidewalk, which is physically infeasible as sidewalks are always below walls. Right: a road segment in the prediction is surrounded completely by sidewalk, which is also physically infeasible.



Figure 2. We can see a part of traffic sign is completely included by wall class in prediction image (right) Cityscapes val set which is an inclusion constraint.

We have performed an empirical analysis (Sec. 4.5) on the labels of the Cityscapes training set and the predictions produced by SegFormer-B4 [26] on Cityscapes val set and have discovered from the ground-truth labels which class pairs correspond to infeasible inclusions and which do not.

1.2. Discontinued Segments

A discontinued or “broken” segment refers to those scenarios where for a particular class, the number of connected segments present in the predicted image is higher than the number of segments present in the corresponding ground truth. Fig. 3 shows a “broken” rider hand, which is evidence of physical anomalies present in the SegFormer-b4 [26] predictions. Left is the ground truth from a Cityscapes validation image and right is the prediction.

PhyFea removes these two physical anomalies by formulating image morphological operations [9] that is selective dilation [9] and area opening [9]. PhyFea does not use any trainable parameters like convolution layer but the custom layers are differentiable while training.

PhyFea takes the raw output of the baseline as input and set a boundary constraint between 0 and 1 to the input. The dimension of the input to PhyFea is (C, H, W) where C is the number of classes present in the dataset and H, W are the usual height and width of the input images. Now if we consider each class pair, then number of all possible pairs are $C * (C - 1)$. PhyFea considers each of these class pair and converts them to a binary feature map where the background pixels will be zero valued and foreground pixels will be the non zero class segments and checks if any segment has inclusion constraint anomaly or discontinued class anomaly.

If any class pair contains inclusion constraint anomaly,



Figure 3. We can see the rider hand is broken in prediction image (right) from Cityscapes validation set. This is a discontinued or “broken” segment, which is clearly infeasible.

PhyFea applies an iterative max-pooling operation as area opening [9] to open the included class segment. Similarly, if a class segment in a pair contains a discontinued class anomaly PhyFea performs an iterative average-pooling and rectification as selective dilation to join the two broken segments. The number of iteration in both opening and selective dilation is determined heuristically so that only physically infeasible inclusion constraint segments are removed and only discontinued class segments get joined. Finally, after opening and selective dilation PhyFea computes two independent functions $\mathbf{H}(\mathbf{P}_\phi(I))$ and $\mathbf{H}'(\mathbf{P}_\phi(I))$ for inclusion constraint and selective dilation respectively (refer to Sec. 3.2.1 and Sec. 3.2.2). The function $\mathbf{H}(\mathbf{P}_\phi(I))$ outputs those class segments which are infeasible in nature and the function $\mathbf{H}'(\mathbf{P}_\phi(I))$ outputs the *dilation-offset* which joins two broken segments of the discontinued class. Then the absolute difference of these outputs are taken and multiplied with a value α and then added to the cross-entropy loss of the baseline to obtain the total loss. The total loss is then backpropagated to optimize the network weights.

We have achieved a significant performance improvement with PhyFea on three central benchmarks for semantic segmentation: ADE20K, Cityscapes, and ACDC. More specifically, we show that applying PhyFea on top of both of the recent state-of-the-art SegFormer [26] and OCRNet [28] networks improves segmentation performance consistently and significantly across all three benchmarks.

2. Related Work

Physical priors using local correlations. Physical domain knowledge in medical domain is implemented specially in MRA, PET, MRI scan images concerns optimizing energy function or implementation in Markov Random Field [13] (a graphical model approach). Other approaches on implementing physical priors in semantic segmentation model is AAF (Adaptive Affinity Field) [11] which is very closely related to CRF (Conditional Random Field) [12]. In AAF, the predicted feature map of PSPNet [30] is compared with the input feature map using multiple sized kernel windows using KL divergence as loss function.

Physical priors via full supervision. Zhang et al. [25] stated that physical priors can be implemented in a neural

framework in four different ways. The first strategy is to integrate constraints into data by generating synthetic training datasets. The second strategy is to design non-trainable custom layers of physical operators and pre-conditioners in the DNN architecture to modify or shape feature maps calculated within the network to make them consistent with the prior knowledge. Implementing physical priors in semantic segmentation network is also done by modern techniques using Self-attention [22]. CCNet [10] is one such example. In CCNet, ResNet-101 is used as backbone to extract feature map and dilated convolution [27] is applied to increase spatial dimension of the feature map. Then using 1-D convolution to obtain the necessary parameters to apply self-attention map the semantic structures. In this model the key factor is applying self-attention to capture the semantic relationships between the classes.

Physical priors in the loss function. Physical priors can be enforced in the loss function as regularization loss as in the Potts model [21] in discrete domain that penalizes appearances discontinuity between neighbouring pixels and is defined as $\sum_{p,q \in N} w_{pq} \delta(I_p \neq I_q)$. The regularization term formulated in the discrete setting is biased by the discrete grid and favours curves to orient along with the grid, e.g. in horizontal and vertical or diagonal directions in a 4-connected lattice of pixels. Previous attempts are made in the implementation of physical priors by incorporating shape information in the architecture. Shape information is a powerful semantic descriptor for specifying targeted objects in an image. Shape prior can be modelled in three ways: geometrical (template-based), statistical, and physical.

There are special types of neural architectures where physical priors can be implemented in loss functions. These types of networks are also called PINNs [17] (Physics Informed Neural Networks). PINNs are basically differential equation solver where a differential equation encodes the physical constraint. The neural network approximates the solution of the equation using boundary constraints. There are studies done in the geophysics domain to implement geophysical priors and laws in deep neural network as regularization terms in loss functions for training the DNNs.

Nosrati et al. [16] conducted a survey of incorporating prior knowledge in medical image segmentation. The paper reviews various ways to device prior knowledge information to improve image segmentation. The said physical priors can be implemented with global or local optimization; also implementation of physical priors in continuous or discrete domain. Rother et al. [18] suggest possible ways to incorporate appearance priors in image segmentation using Gaussian mixture models [18]. In the literature, there are two ways to model the appearance: 1) learning the appearance in adaptive manner during the segmentation procedure, and 2) knowing the appearance model prior

to performing segmentation (e.g. by observing the appearance distribution of the training data). In the former case, the appearance model is learned as the segmentation is performed, Vese and Chan, 2002 [23] (computed online). In the second case, it is assumed that the probability of each pixel belonging to particular label is known, i.e. if $F_i(x)$ represents a particular set of feature values (e.g. intensity/color) associated with each image location for i^{th} object, then it is assumed that $P(x/F_i(x))$ is known (or pre-computed offline). This probability is usually learned and estimated from the distribution of features inside small samples of each object. To fit the segmentation appearance distribution to the prior distribution, a dissimilarity measure d is usually needed where $d(g_i, \hat{g}_i)$ measures the difference between the appearance distribution of the i^{th} object (g_i) and its corresponding prior distribution \hat{g}_i . This dissimilarity measure can be encoded into the energy function $S^* = \arg \min_s \lambda * R * (S) + D(S; I)$ where, S^* represent the set of all optimal solutions. R is the regularization term which enforces the physical priors. D is the data term which represents the strength of the association of a pixel with a label. $D(S; I)$ represents the strength factor of association for a given solution of a particular image, either directly as the data term or via a probabilistic formulation.

Comparison of our method with the related works. All the above methods to enforce physical priors into a deep neural architecture do not take into account the semantic relation among the classes in the image. For example for outdoor scenes, sky should be above the road or a road cannot be completely surrounded by sidewalk or sidewalk cannot be surrounded by the wall of a building. Similarly, other scenarios, which can be observed sometimes in the prediction feature map of 2D semantic segmentation models is like there is a presence of discontinuity in the class segments. For example a rider class or a person class has a discontinued body part which is also physically infeasible. This shows that during training the model; it is not being trained keeping in mind with all these semantic relations among the classes. PINN [17] though take into account the shape priors and being used in medical domain for image segmentation, it cannot be used for semantic segmentation for outdoor scenes. Because, we cannot enforce a fixed structure of any class in outdoor scenes unlike fixed shape anatomical structures like brain, heart veins etc. which is required to formulate the differential equation which is later approximated by the PINN [17].

3. Method

3.1. Method Overview

Fig. 4 shows the architectural overview of PhyFea. A 2D semantic segmentation model as baseline network $\phi(X)$ takes an image $\mathbf{I} \in \mathbb{R}^{(3,H,W)}$ as input and produces the

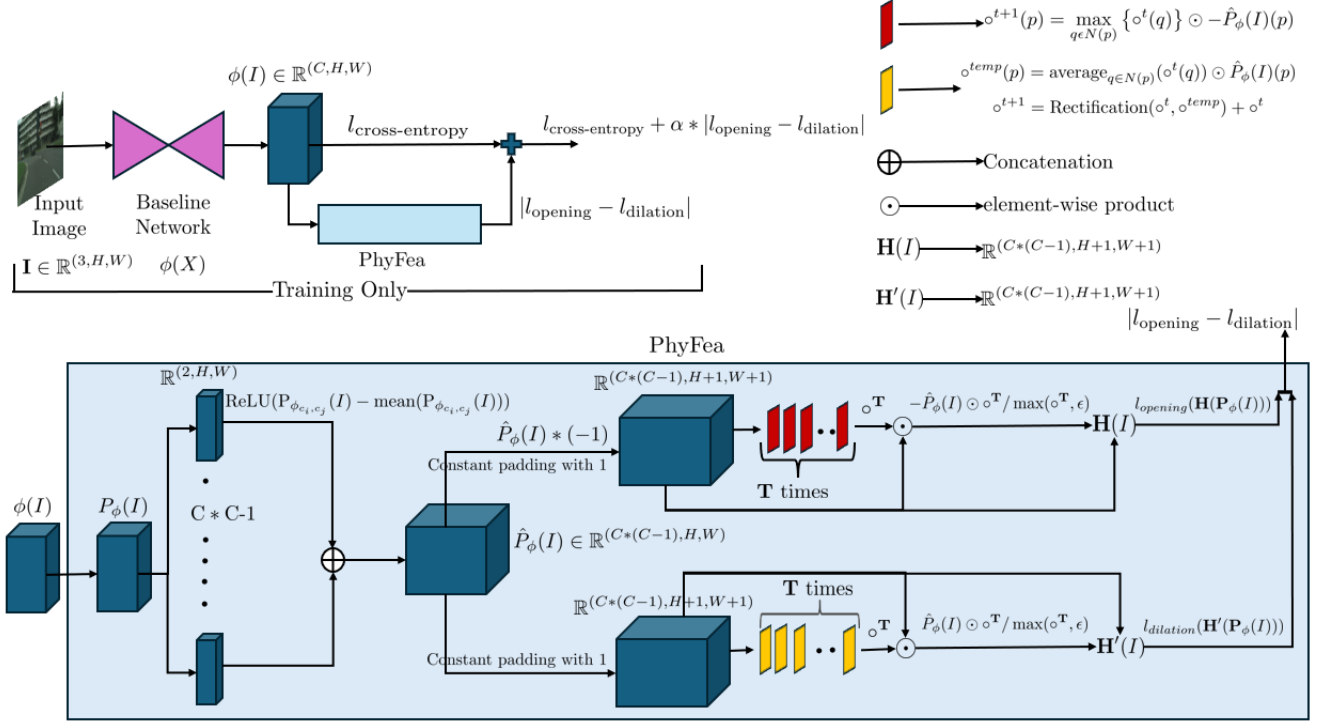


Figure 4. **Overview of PhyFea.** Top left: illustration of the complete network architecture, where the cross-entropy loss of the baseline network is added to the losses of PhyFea. Bottom: the pipeline of PhyFea, where red-colored boxes are iterations for opening and yellow-colored boxes are for selective dilation. Top right: legends for various components of PhyFea, such as the operations we apply in iterative manner for area opening and for selective dilation and the two functions to calculate the losses.

raw output $\phi(I) \in \mathbb{R}^{(C,H,W)}$ where C is the number of classes present in the dataset. PhyFea takes $\phi(I)$ as input and produces an absolute difference of two loss values $l_{opening}$ and $l_{dilation}$ generated by the two operations performed in PhyFea, namely opening and selective dilation. Opening solves the inclusion constraint problem and selective dilation solves the discontinued class problem. The absolute difference $|l_{opening} - l_{dilation}|$ is then added to the cross-entropy loss (denoted by $l_{cross-entropy}$) of $\phi(X)$ to obtain the total loss (i.e. Eq. 1), here α is a hyperparameter and it is used to balance the loss of PhyFea and the baseline network. $l_{total-loss}$ is backpropagated to optimize the weights of the baseline network by obtaining the argmin of $l_{total-loss}$. PhyFea is end-to-end differential in order to incorporate the physical priors (i.e. Inclusion constraint and discontinued class) while re-training the baseline network and it is free of any parameterized component like convolution kernel or MLP.

$$l_{total-loss} = l_{cross-entropy} + \alpha * |l_{opening} - l_{dilation}|, 0 < \alpha < 1 \quad (1)$$

$$S^* = \underset{s}{\operatorname{argmin}} (l_{total-loss})$$

3.2. PhyFea

PhyFea takes $\phi(I)$ as input and transform it to $P_\phi(I)$ such that $0 \leq P_\phi(I) \leq 1$. PhyFea divides $P_\phi(I)$ into $C * (C - 1)$ class pairs. For each class pair $P_{\phi_{c_i}, c_j}(I)$ where $i, j \in \mathbb{Z}^+$ and $1 \leq i, j \leq C$ and $i \neq j$. PhyFea perform $\operatorname{ReLU}(P_{\phi_{c_i}, c_j}(I) - \operatorname{mean}(P_{\phi_{c_i}, c_j}(I)))$. This operation helps in achieving a binary feature map where background pixels are zero and foreground pixels are non-zero class segments; necessary for performing grey scale opening and selective dilation (since, $\operatorname{mean}(P_{\phi_{c_i}, c_j}(I))$ will always lie between $P_{\phi_{c_i}}$ and $P_{\phi_{c_j}}$, so after subtracting the mean and applying ReLU; only those non-zero pixels will remain which are greater than the mean value). Now all these $C * (C - 1)$ class-pairs are concatenated to obtain an intermediate feature map $\hat{P}_\phi(I) \in \mathbb{R}^{(C*(C-1), H, W)}$. (Refer equation 2)

$$\hat{P}_\phi(I) = \sum_{i=1}^C \sum_{j=1}^C (\operatorname{ReLU}(P_{\phi_{c_i}, c_j}(I) - \operatorname{mean}(P_{\phi_{c_i}, c_j}(I)))) \quad (2)$$

PhyFea applies opening (Sec. 3.2.1) and selective dilation (Sec. 3.2.2) on $\hat{P}_\phi(I)$ separately and compute the two loss functions $l_{opening}$ and $l_{dilation}$ (Sec. 3.1).

3.2.1 Opening

In order to perform area opening of any class segment belonging to a class pair C_i, C_j first $\hat{P}_\phi(I)$ is multiplied with -1 so that the non-zero foreground class segments become negative valued and a constant padding of 1 is added (Refer to Sec. 3.2.3). If any segment belongs to inclusion constraint, PhyFea opens the segment by an iterating process of max-pooling (since foreground is negative valued and background is zero so max-pooling will remove the foreground pixels) succeeded by an element-wise product with $-\hat{P}_\phi(I)$ as shown in Eq. 3.

$$\circ^{t+1}(p) = \max_{q \in N(p)} \{ \circ^t(q) \} \odot -\hat{P}_\phi(I)(p) \quad (3)$$

PhyFea performs the iteration T times. The value of T is decided heuristically. $T = \max(2, \max(H, W)/2)$ where H and W are the usual height and width of the input image (the iteration formula is set as the half of the maximum side of the feature map to achieve better convergence). The final result of iteration i.e. \circ^T is normalized and succeeded by element-wise product with $-\hat{P}_\phi(I)$. Finally the result of the product and $-\hat{P}_\phi(I)$ is passed to the function $H(I)$ (as shown in Eq. 4).

$$H(I) = -\hat{P}_\phi(I) - (-\hat{P}_\phi(I) \odot \circ^T / \max(\circ^T, \epsilon)) \quad (4)$$

So, $H(\mathbf{P}_\phi(I)) \in \mathbb{R}^{C*(C-1), H, W}$. $H(\mathbf{P}_\phi(I))$ is zero if C_i, C_j has no segment which falls under inclusion constraint and is a physical anomaly otherwise it is non-zero. Finally, l^1 norm is taken of the $H(\mathbf{P}_\phi(I))$ which is denoted as l_{opening} .

More clarifications on $H(\mathbf{P}_\phi(I))$: The function has 2 components. If there exists a class pair C_i, C_j which has say k segments s_1, s_2, \dots, s_k where let say s_2 is a physical anomaly belongs to inclusion constraint. Now $-\hat{P}_\phi(I)$ will contain all the k segments. $(-\hat{P}_\phi(I) \odot \circ^T / \max(\circ^T, \epsilon))$ will not contain the anomaly segment s_2 (since we have heuristically determined that if we apply the iteration operation T times it will successfully remove the anomaly segments). Therefore, $H(\mathbf{P}_\phi(I))$ will be equal to the segment s_2 . PhyFea penalizing this anomaly segment by taking l^1 norm along with the cross-entropy loss and l_{dilation} (which is shown in Eq. 1).

3.2.2 Selective dilation

In order to perform selective dilation on two broken segments of a class in a class-pair, first $\hat{P}_\phi(I)$ is padded with constant value 1 (Refer to Sec. 3.2.3). PhyFea joins two broken segment by an iterating process of average-pooling succeeded by element-wise product with $\hat{P}_\phi(I)$ (as shown in Eq. 5) and then passing the result of the product to a function called **Rectification**. Rectification further fine-tune the *dilation-offset* (i.e. $\circ^{temp} - \circ^t$).

Further clarification on the functionality of average pooling: Let there exists a discontinued class anomaly in a class of a pair in $\hat{P}_\phi(I)$. Let that particular class have k segments s_1, s_2, \dots, s_k where let say s_3 and s_4 are two broken segments required to be joined and they are at a close proximity with each other at a particular edge point E_p .

Now we are applying iterative average-pooling operation. When average-pooling is applied at E_p we get the average like $\text{Ave}_1 = \text{average}(P_{s_3}, P_{s_4}, 0, 0, \dots)$ where P_{s_3} is the pixel from segment s_3 and P_{s_4} is the pixel from segment s_4 and 0's are the background pixels. When the average-pooling is applied to other edge regions of the segments we get the average like $\text{Ave}_2 = \text{average}(P_{s_x}, 0, 0, 0, \dots)$ where P_{s_x} can be any pixel in either segment s_3 or s_4 .

It is evident that $\text{Ave}_1 > \text{Ave}_2$. So, while performing Rectification; only Ave_1 will exist and Ave_2 will become 0. In this way, we are selectively dilating the segments only at E_p .

Rectification: This function performs the similar operations of applying ReLU on the difference of *dilation-offset* and it's mean value succeeded by adding the result to \circ^t (as shown in Eq. 5). The reason behind the functionality of Rectification is we are modifying the structure of the *dilation-offset* before adding it to the \circ^t in such a way that the dilation will be existent only at that particular edge point where the two broken segments are in close proximity.

$$\circ^{temp}(p) = \text{average}_{q \in N(p)} (\circ^t(q)) \odot \hat{P}_\phi(I)(p)$$

$$\circ^{t+1} = \text{Rectification}(\circ^t, \circ^{temp}) \text{ where}$$

Rectification

$$= \text{ReLU}((\circ^{temp} - \circ^t) - \text{mean}(\circ^{temp} - \circ^t)) + \circ^t \quad (5)$$

PhyFea performs the iteration T times similar to opening operation. The final result of iteration i.e. \circ^T is normalized and succeeded by element-wise product with $\hat{P}_\phi(I)$. Finally the result of the product and $\hat{P}_\phi(I)$ is passed to the function $H'(I)$ (as shown in Eq. 6).

$$H'(I) = \hat{P}_\phi(I) - \hat{P}_\phi(I) \odot \circ^T / \max(\circ^T, \epsilon) \quad (6)$$

So, $H'(\mathbf{P}_\phi(I)) \in \mathbb{R}^{C*(C-1), H, W}$. $H'(\mathbf{P}_\phi(I))$ is zero if C_i, C_j has no segment which falls under discontinued class anomaly otherwise it is non-zero. Finally, l^1 norm is taken of the $H'(\mathbf{P}_\phi(I))$ which is denoted as l_{dilation} .

More clarifications on $H'(\mathbf{P}_\phi(I))$: It has 2 components. If there exists a class pair C_i, C_j which has say k segments s_1, s_2, \dots, s_k where let say s_3 and s_4 are two broken segments i.e. they should belong to only one segment. Now, $\hat{P}_\phi(I)$ contains all the k segments and $\hat{P}_\phi(I) \odot \circ^T / \max(\circ^T, \epsilon)$ contains $k - 1$ segments (since after T iterations two broken segments will join). Therefore, $H'(\mathbf{P}_\phi(I))$ will contain only the joining bridge between s_3

and s_4 . Similar to opening, l^1 norm is taken and penalized with cross-entropy loss and l_{opening} (refer to Eq. 1).

3.2.3 Explanation of functionality of constant padding with 1 for intermediate feature map

In order to perform opening and selective dilation it is mentioned that the intermediate feature map $\hat{P}_\phi(I)$ is padded with constant value 1. The reason behind this is that we want to restrict the two operations to the central region of the feature map. When we mention inclusion constraint anomaly, it means that the included segment is surrounded by another class segment so, the included segment cannot share border pixels.

Similarly, for discontinued class anomaly we observe that the broken segments lie in the central region of the images. That is why for both of the operations we set the border pixels with a high value of 1 so that the border pixels remain unaffected by max-pooling and average-pooling operations.

4. Experiments

4.1. Datasets

Cityscapes. We have used the dataset Cityscapes [7]. It is a driving dataset, containing various outdoor images of various cities in Europe. The dataset contains 2975 train images and fine annotated images. 500 validation train images and fine annotated images and 20k train-coarse annotation images (weakly annotated). Several hundreds of thousands of frames were acquired from a moving vehicle during the span of several months, covering spring, summer, and fall in 50 cities, primarily in Germany but also in neighboring countries. Adverse conditions are recorded.

ADE20K. We have used the dataset ADE20K [32]. It was earlier used in ImageNet scene parsing challenge 2016. There are 150 classes and diverse scenes with 1038 image-level labels. The dataset is divided into 20K/2K/3K images for training, validation and test set.

ACDC. We have used the dataset ACDC [19] (The Adverse Conditions Dataset with Correspondences for Semantic Driving Scene Understanding). it is a dataset consists of driving scenes under adverse conditions like fog, night, rain and snow. It has 19 classes similar to the Cityscapes [7] dataset. The dataset is divided into 1600 train set, 406 validation set and 2000 test set.

4.2. Implementation Details

Training setup. We used mmsegmentation [6] for the baseline network SegFormer-B4 and used their pretrained model. For OCRNet, their official implementation is taken and their pretrained model. For the experiments done on

Table 1. **Comparison with state-of-the-art semantic segmentation methods on ADE20K, Cityscapes and ACDC.** ‘*’: multi-scale testing. Results are reported on Cityscapes test set, ADE20K val set and ACDC test set. None of HRNet, SegFormer and OCRNet are not jointly trained on Cityscapes and ACDC.

Method \ Dataset	ADE20K (mIoU)	Cityscapes (mIoU)	ACDC (mIoU)
PSPNet [30]	44.4	78.5	-
DeepLabv2 [3]	-	71.4	47.1
DeepLabv3+ [4]	44.1	80.9	41.6
HRNet [26]	43.1	80.9	35.3
Mask2Former [5]	47.2	83.3	76.2
OCRNet (baseline) [28]	44.9*	82.3*	51.1
PhyFea (ours)	45.9*	83.0*	66.9
SegFormer-B4 (baseline) [26]	49.7	82.2	67.1
PhyFea (ours)	51.2	82.8	69.2

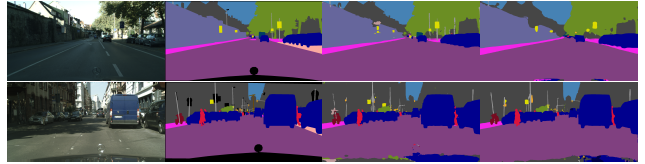


Figure 5. **Qualitative comparison on Cityscapes.** From left to right: input image, ground-truth semantic labels, and predictions of baseline SegFormer network and of PhyFea (ours).

SegFormer-B4 [26], we have done random cropping of the input images to size 1024×1024 on Cityscapes [7], and 512×512 on ADE20k [32] and 1024×1024 for ACDC [19] dataset. We have used a Batch size of 4 on Cityscapes and ACDC dataset and 16 for ADE20K. Optimizers, number of iterations and learning rate parameters used is same as in SegFormer [26]. OHEM [20] is not used. Random resizing with ratio 0.5-2.0 is done. Other data augmentation techniques like random flipping is also used.

For OCRNet [28] without SegFix [28], OHEM [20] is not used. Neither any auxiliary loss is used in implementation. Various data augmentation methods including colour augmentation, horizontal flipping is done. For Cityscapes 769×769 crop size is used, for ADE20k [32] 520×520 cropping is used and for ACDC [19] 780×780 cropping is used. Here also batch size 8 used for Cityscapes and ACDC, 16 for ADE20K. Optimizers, number of iterations and learning rate used for OCRNet [28] is same as mentioned in the original paper. We report semantic segmentation performance using mean Intersection over Union (mIoU). The value of α is decided using random search from the set $[1e-5, 1e-10]$. We have used 4 GPUs each with memory greater than 20GB for both baselines.

4.3. Comparisons to The State of The Art

Tab. 1 shows the mIoU scores of different models including ours on 3 datasets. SegFormer-B4 [26] refers to SegFormer with Encoder MiT-B4 [26]. **m.s.** refers to multi scale testing. Every model is tested in single scale unless mentioned otherwise. We can observe an 0.6% improve-

Table 2. **Comparison of class-level IoU between the baseline models OCRNet (top) or SegFormer-B4 (bottom), respectively, and PhyFea on the Cityscapes val set.** Training and evaluation are performed using the complete training and val sets, respectively.

Method	road	sidew.	build.	wall	fence	pole	light	sign	veget.	terrain	sky	person	rider	car	truck	bus	train	motorc.	bicycle	mIoU
Baseline	96.4	88.2	95.7	68.2	57.7	69.6	74.5	81.6	93.1	66.8	95.4	84.8	68.3	95.6	81.8	90.7	83.9	73.6	80.0	81.3
Ours	98.2	91.3	93.8	73.1	52.2	56.2	73.5	79.3	93.5	74.0	93.8	85.0	74.8	95.7	90.8	95.2	84.7	83.3	79.1	82.5
Baseline	98.4	87.2	93.7	68.2	65.4	69.6	74.5	81.6	93.1	70.6	95.4	84.8	68.3	95.6	81.8	90.7	83.9	73.6	80.0	81.9
Ours	99.2	91.3	93.8	72.1	72.3	56.2	73.5	79.3	93.5	74.0	93.8	85.0	74.8	95.7	90.8	95.2	84.7	83.3	79.1	83.6

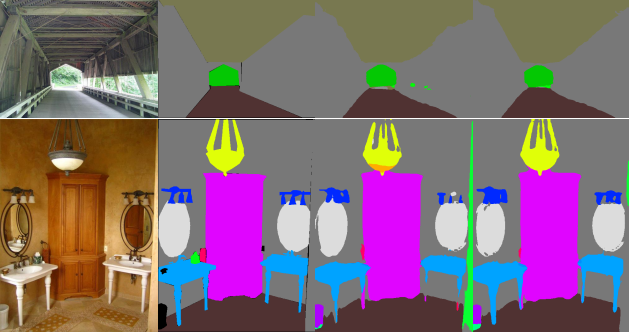


Figure 6. **Qualitative comparison on ADE20K.** From left to right: input image, ground-truth semantic labels, and predictions of baseline OCRNet network and of PhyFea (ours).

ment in mIoU score in Cityscapes [7] test set on SegFormer-B4 [26] baseline and 0.7% improvement on the OCRNet [28] baseline. PhyFea achieves 1.02% improvement on the baseline OCRNet for ADE20K [32] dataset and 1.44% on the baseline SegFormer-B4. PhyFea achieves 15.77% improvement on the baseline OCRNet for ACDC dataset and 2.17% on the baseline SegFormer-B4. We can observe that Mask2Former has the highest mIoU score across all the 3 datasets. PhyFea able to gain improvement on the respective baselines on all the 3 datasets by enforcing the two physical constraints but PhyFea is baseline independent. It means it can improve the image segmentation of a given baseline network on which it is applied by enforcing the physical constraints.

Table 2 is the class-wise comparison of IoU on Cityscapes [7] val set for PhyFea and the corresponding baselines. We can observe that PhyFea achieved an overall improvement in IoU scores across the classes. However, there is a decrease in IoU values in some classes especially in Pole class for both of the baselines. This is due to the reason that Pole class do not share any border pixels in the images. In other words, PhyFea confuses Pole class with a inclusion constraint anomaly. We can also observe this effect on Pole class in the Cityscapes predicted images of the baseline after re-training it with PhyFea.

Table 3 is the class-wise comparison of IoU on

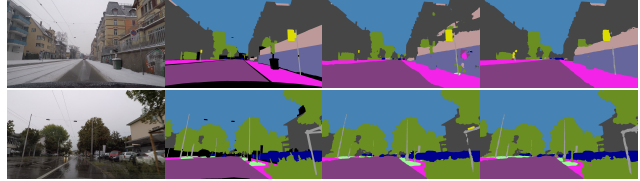


Figure 7. **Qualitative comparison on ACDC.** From left to right: input image, ground-truth semantic labels, and predictions of baseline SegFormer network and of PhyFea (ours).

ACDC [19] test set for PhyFea and the corresponding baselines. Here also we can observe that PhyFea achieved an overall improvement in IoU scores across the classes specially over the OCRNet baseline. But unlike, in Cityscapes validation set, the Pole class has gained IoU score significantly after re-training the baselines with PhyFea. Though ACDC dataset is an adaptation of the Cityscapes dataset under adverse weather conditions like fog, snow, night time etc. we observe no decrease in IoU score for the Pole class.

The difference of IoU scores that we observe in different datasets is directly influenced by the number of iterations PhyFea use for inclusion constraint and discontinued class anomaly. As, the number of iterations is set heuristically, we calibrated the iteration formula in such a way that we achieved an improvement in overall mIoU in all the three datasets.

Cityscapes results: In Fig. 5 We can see on the left(in the baseline prediction image) that a segment of traffic sign included by wall which is an infeasible inclusion constraint and we have successfully opened the segment of the traffic sign. We can see in baseline prediction image that a person to the left has a broken foot and another person to the right has his head detached from the body which is infeasible. And we have successfully dilated to bridge the gaps of the person class. But in all the two sets of predictions we can observe that the Pole class segments have been shrunked drastically in the final PhyFea re-trained images.

ADE20K results: In Fig. 6, the baseline prediction in the top row, a segment of vegetation is incorrectly included by another class, while PhyFea successfully opens the former segment. In the bottom row, the legs of the sink in the

Table 3. Comparison of class wise IoU between the baseline model OCRNet and SegFormer-B4 and our implementation on ACDC test from top to bottom respectively. Training and evaluation are performed using the complete training and test sets, respectively.

Method	road	sidew.	build.	wall	fence	pole	light	sign	veget.	terrain	sky	person	rider	car	truck	bus	train	motorc.	bicycle	mIoU
Baseline	85.9	58.4	77.9	28.6	32.8	39.9	53.1	49.0	74.7	42.2	89.2	49.5	21.1	72.7	34.5	38.0	65.2	20.3	38.3	51.1
Ours	94.4	77.8	88.1	49.9	46.2	48.9	61.4	62.3	85.5	59.6	95.5	58.5	40.5	87.4	63.6	76.3	80.7	41.7	53.2	66.9
Baseline	94.6	78.3	88.4	51.6	47.4	48.0	62.1	61.2	87.0	66.8	95.6	59.8	39.0	87.0	63.1	73.8	79.1	38.4	52.7	67.1
Ours	94.8	79.5	88.5	54.2	50.4	48.7	63.7	64.2	87.9	66.2	95.9	61.2	42.0	88.2	70.8	77.9	84.1	42.3	54.6	69.2

Table 4. Empirical analysis on Cityscapes validation set ground-truth labels and predictions of SegFormer-B4.

Values \ Set	Ground Truth (%)	Prediction (%)
Non-Constraint pairs	67.9	61.3
Constraint Pairs	32.1	38.7
Feasible Pairs	97.1	89.6
Infeasible Pairs	2.9	10.4

baseline prediction are discontinued, PhyFea able to join the discontinued segments.

ACDC results: In Fig. 7 we can see in baseline prediction that some segments of sidewalk class is included by wall class. And we have successfully opened those segments. We can see in baseline prediction image that some segments of pole class is broken/discontinued which is removed in the final retrained image. As already discussed earlier, here in ACDC dataset we can see there is no degradation in the Pole class segments in the predicted images produced after PhyFea re-training.

4.4. Ablation Study

We performed an ablation study on SegFormer-B4 [26] baseline using Cityscapes [7] validation set as test. We used one loss at a time for the ablation study. For $l_{opening}$ mIoU is 81% which is same as the mIoU for the baseline network without using PhyFea. This shows that although PhyFea able to solve the inclusion constraint anomalies, it does not take into account the discontinued class constraint and as a result we have not observed any significant improvement in the mIoU score. For $l_{dilation}$ we have observed a mIoU score of 78.8% which is even lesser than the reported mIoU score of the baseline network. Our ablation study evidences that for Cityscapes validation set, the number of inclusion constraint anomalies is more than the number of discontinued class anomalies across all possible class pairs. From Sec. 4.5 we have observed that among all the inclusion constraint in prediction only 10.4% is falling under the anomaly. So the amount of discontinued class anomalies should be less than inclusion constraint anomalies.

4.5. Empirical Analysis

We have done some empirical analysis on the Cityscapes ground truth train set and on the SegFormer-B4 [26] prediction on val set (refer to Tab. 4). We checked the number of inclusion constraint pairs termed as **”Constraint Pairs”** in both ground truth and on prediction. Then we check among those **”Constraint Pairs”** how many are having infeasible scenarios termed as **”Infeasible Pairs”** in ground truth as well as in the prediction. **”Non Infeasible Pairs”** refer to those inclusion constraint pairs which do not violate the physical world rules. We also checked among 342 class pairs how many class pair co-occur across all images in train set and validation set and found that all the 342 possible pairs co-occur. It means that for any given class pair there exists at least one image in both train and val set. **”Non-Constraint pairs”** are those co-occurring pairs which do not fall under the inclusion constraint category. We can observe that the percentage of **”Infeasible Pairs”** is very less in both ground truth and in prediction as compared to the total percentage of **”Constraint Pairs”**. We ignored the infeasible pairs in ground truth as it is very negligible percentage and considered as labeling error. Anomaly in ground truth is in Supplementary paper.

5. Conclusion and Future Work

In this paper we did not build any new semantic segmentation architecture. Rather we tried to enhance the prediction of an existing neural network by enforcing few physical priors into the network. We took two existing well-known semantic segmentation models and enforced the physical priors like inclusion constraint and discontinued class. In most of the cases we are able to achieve our goal, however in few cases we have observed that final prediction feature map have some classes which got shrunk specially those classes which do not share border pixels. For example pole class in Cityscapes [7] which is a scope of future work where we can prevent PhyFea to open these types of classes which do not share boundary pixels. In overall scenario, we are successful in attaining our goal significantly in both quantitative and qualitative way.

References

- [1] Liang-Chieh Chen, George Papandreou, Iasonas Kokkinos, Kevin Murphy, and Alan L. Yuille. Semantic image segmentation with deep convolutional nets and fully connected crfs, 2016. **1**
- [2] Liang-Chieh Chen, George Papandreou, Iasonas Kokkinos, Kevin Murphy, and Alan L. Yuille. Deeplab: Semantic image segmentation with deep convolutional nets, atrous convolution, and fully connected crfs, 2017. **1**
- [3] Liang-Chieh Chen, George Papandreou, Iasonas Kokkinos, Kevin Murphy, and Alan L. Yuille. Deeplab: Semantic image segmentation with deep convolutional nets, atrous convolution, and fully connected crfs, 2017. **6**
- [4] Liang-Chieh Chen, Yukun Zhu, George Papandreou, Florian Schroff, and Hartwig Adam. Encoder-decoder with atrous separable convolution for semantic image segmentation, 2018. **6**
- [5] Bowen Cheng, Ishan Misra, Alexander G. Schwing, Alexander Kirillov, and Rohit Girdhar. Masked-attention mask transformer for universal image segmentation, 2022. **6**
- [6] MMSegmentation Contributors. MMSegmentation: Openmmlab semantic segmentation toolbox and benchmark. <https://github.com/open-mmlab/mms Segmentation>, 2020. **6**
- [7] Marius Cordts, Mohamed Omran, Sebastian Ramos, Timo Rehfeld, Markus Enzweiler, Rodrigo Benenson, Uwe Franke, Stefan Roth, and Bernt Schiele. The cityscapes dataset for semantic urban scene understanding, 2016. **1, 6, 7, 8**
- [8] Alexey Dosovitskiy, Lucas Beyer, Alexander Kolesnikov, Dirk Weissenborn, Xiaohua Zhai, Thomas Unterthiner, Mostafa Dehghani, Matthias Minderer, Georg Heigold, Sylvain Gelly, Jakob Uszkoreit, and Neil Houlsby. An image is worth 16x16 words: Transformers for image recognition at scale, 2021. **1**
- [9] Rafael Corsino González, Richard E. Woods, and Barry R. Masters. Digital image processing, third edition. *Journal of Biomedical Optics*, 14:029901, 2009. **2**
- [10] Zilong Huang, Xinggang Wang, Yunchao Wei, Lichao Huang, Humphrey Shi, Wenyu Liu, and Thomas S. Huang. Cnet: Criss-cross attention for semantic segmentation, 2020. **3**
- [11] Tsung-Wei Ke, Jyh-Jing Hwang, Ziwei Liu, and Stella X. Yu. Adaptive affinity fields for semantic segmentation, 2018. **2**
- [12] Philipp Krähenbühl and Vladlen Koltun. Efficient inference in fully connected crfs with gaussian edge potentials, 2012. **2**
- [13] Ziwei Liu, Xiao Xiao Li, Ping Luo, Chen Change Loy, and Xiaoou Tang. Deep learning markov random field for semantic segmentation, 2017. **2**
- [14] Ze Liu, Yutong Lin, Yue Cao, Han Hu, Yixuan Wei, Zheng Zhang, Stephen Lin, and Baining Guo. Swin transformer: Hierarchical vision transformer using shifted windows, 2021. **1**
- [15] Jonathan Long, Evan Shelhamer, and Trevor Darrell. Fully convolutional networks for semantic segmentation, 2015. **1**
- [16] Masoud S. Nosrati and Ghassan Hamarneh. Incorporating prior knowledge in medical image segmentation: a survey, 2016. **3**
- [17] M. Raissi, P. Perdikaris, and G.E. Karniadakis. Physics-informed neural networks: A deep learning framework for solving forward and inverse problems involving nonlinear partial differential equations. *Journal of Computational Physics*, 378:686–707, 2019. **3**
- [18] Carsten Rother, Vladimir Kolmogorov, and Andrew Blake. "grabcut": Interactive foreground extraction using iterated graph cuts. *ACM Trans. Graph.*, 23(3):309–314, aug 2004. **3**
- [19] Christos Sakaridis, Dengxin Dai, and Luc Van Gool. ACDC: The adverse conditions dataset with correspondences for semantic driving scene understanding. In *Proceedings of the IEEE/CVF International Conference on Computer Vision (ICCV)*, October 2021. **6, 7**
- [20] Abhinav Shrivastava, Abhinav Gupta, and Ross Girshick. Training region-based object detectors with online hard example mining, 2016. **6**
- [21] Andrea Tirelli, Danyella O. Carvalho, Lucas A. Oliveira, José P. de Lima, Natanael C. Costa, and Raimundo R. dos Santos. Unsupervised machine learning approaches to the q-state potts model. *The European Physical Journal B*, 95(11), Nov. 2022. **3**
- [22] Ashish Vaswani, Noam Shazeer, Niki Parmar, Jakob Uszkoreit, Llion Jones, Aidan N Gomez, Ł ukasz Kaiser, and Illia Polosukhin. Attention is all you need, 2017. **3**
- [23] Luminia Vese and Tony Chan. A multiphase level set framework for image segmentation using the mumford and shah model. *International Journal of Computer Vision*, 50, 07 2004. **3**
- [24] Wenhai Wang, Enze Xie, Xiang Li, Deng-Ping Fan, Kaitao Song, Ding Liang, Tong Lu, Ping Luo, and Ling Shao. Pyramid vision transformer: A versatile backbone for dense prediction without convolutions, 2021. **1**
- [25] Xinming Wu, Jianwei Ma, Xu Si, Zhengfa Bi, Jiarun Yang, Hui Gao, Dongzi Xie, Zhixiang Guo, and Jie Zhang. Sensing prior constraints in deep neural networks for solving exploration geophysical problems. *Proceedings of the National Academy of Sciences*, 120(23):e2219573120, 2023. **2**
- [26] Enze Xie, Wenhai Wang, Zhiding Yu, Anima Anandkumar, Jose M. Alvarez, and Ping Luo. Segformer: Simple and efficient design for semantic segmentation with transformers, 2021. **1, 2, 6, 7, 8**
- [27] Fisher Yu and Vladlen Koltun. Multi-scale context aggregation by dilated convolutions, 2016. **1, 3**
- [28] Yuhui Yuan, Xiaokang Chen, Xilin Chen, and Jingdong Wang. Segmentation transformer: Object-contextual representations for semantic segmentation, 2021. **1, 2, 6, 7**
- [29] Hang Zhang, Chongruo Wu, Zhongyue Zhang, Yi Zhu, Haibin Lin, Zhi Zhang, Yue Sun, Tong He, Jonas Mueller, R. Manmatha, Mu Li, and Alexander Smola. Resnest: Split-attention networks, 2020. **1**
- [30] Hengshuang Zhao, Jianping Shi, Xiaojuan Qi, Xiaogang Wang, and Jiaya Jia. Pyramid scene parsing network, 2017. **2, 6**

- [31] Sixiao Zheng, Jiachen Lu, Hengshuang Zhao, Xiatian Zhu, Zekun Luo, Yabiao Wang, Yanwei Fu, Jianfeng Feng, Tao Xiang, Philip H. S. Torr, and Li Zhang. Rethinking semantic segmentation from a sequence-to-sequence perspective with transformers, 2021. 1
- [32] Bolei Zhou, Hang Zhao, Xavier Puig, Tete Xiao, Sanja Fidler, Adela Barriuso, and Antonio Torralba. Semantic understanding of scenes through the ade20k dataset, 2018. 6, 7